Direction-dependent bending resistance of 3D printed bio-inspired composites with asymmetric 3D articulated tiles

Bioinspiration & Biomimetics

PAPER

Direction-dependent bending resistance of 3D printed bio-inspired composites with asymmetric 3D articulated tiles

Richard J Nash and Yaning Li*

Department of Mechanical and Industrial Engineering, Northeastern University, Boston, MA 02215, United States of America
* Author to whom any correspondence should be addressed.

E-mail: y.li@northeastern.edu

Keywords: tiled composites, additive manufacturing, finite element, bending

Supplementary material for this article is available online

OPEN ACCESS

RECEIVED
28 January 2024

REVISED
25 May 2024

ACCEPTED FOR PUBLICATION
3 July 2024

PUBLISHED
15 July 2024

Abstract

Inspired by the protective armors in nature, composites with asymmetric 3D articulated tiles attached to a soft layer are designed and fabricated via a multi-material 3D printer. The bending resistance of the new designs are characterized via three-point bending experiments. Bending rigidity, strength, and final deflection of the designs are quantified and compared when loaded in two different in-plane and two different out-of-plane directions. It is found that in general, the designs with articulated tiles show direction-dependent bending behaviors with significantly increased bending rigidity, strength, and deflection to final failure in certain loading directions, as is attributed to the asymmetric tile articulation (asymmetric about the mid-plane of tiles) and an interesting sliding-induced auxetic effect. Analytical, numerical, and experimental analyses are conducted to unveil the underlying mechanisms.

1. Introduction

Many natural armors are composed of articulated building blocks bonded on a soft deformable layer to provide both protection and flexibility to accommodate various functions in everchanging environment [1–5]. Examples of these tiled composites in nature include the suture tessellation on the seedcoats of common millets [6, 7], the shell of the red-eared slider turtle [8], various fish armors, such as the alligator gar [9], the striped bass [10], salmon and many more [11–13]. They have been found to have increased stiffness, toughness, and durability under different types of loadings [14–16].

Bending resistance is an important mechanical property for both protection, flexibility, and other functionalities. For example, the seedcoat of portulaca and common millet are composed of jigsaw puzzle-like epidermis cells attaching to a soft cellular layer [17, 18] to protect the seed and to facilitate germination as well. The out-of-plane loads can come from either outside, such as the predator, or inside, such as the germinating seed. Also due to the tessellation, the seedcoat often shows in-plane anisotropy [6]. All these will cause the direction-dependent bending resistance of the corresponding bio-inspired designs.

In this study, inspired by natural tiled composites, we took the approach of designing periodic mechanical metamaterials to design the bio-inspired tiled composites. Then we explore the direction-dependent bending resistance of the periodic dual-layer designs and the mechanisms behind it. Various bioinspired layered composites have been designed to mimic the excellent properties observed in nature such as mimicking the behavior of tissue [19, 20], while some have been designed to improve properties, such as dissipating energy while both increasing strength and diffusing damage under bending [21, 22], both strain to failure and toughness [23], puncture resistance [24], and peel strength [25]. Many engineered metamaterials have been designed to achieve specific and unique properties that usually are not found in nature [26–32]. They can also have enhanced strength, stiffness, toughness, auxetic behavior, and be light weight [33–43]. These materials have geometric or structural geometric properties that can be tuned to obtain the desired set of

mechanical properties [44–51]. A typical approach is to explore the mechanisms through periodic designs.

In this paper, for comparison, both articulated and non-articulated periodic dual-layer tiled composites are designed. The designs are fabricated via a multi-material 3D printer (Stratasys, Objet Connex3). First, uniaxial tension experiments are performed on 3D printed samples to obtain an initial understanding of the direction-dependent stress-strain behaviors of the designs. Then, an analytical model was developed to explore the relationship between the local interacting forces and the degree of articulation, and therefore to unveil the mechanism of increased bending strength for the articulated designs. Finally, three-point bending experiments are performed on the 3D printed designs in two different in-plane directions and two out-of-plane directions. The results are compared to unveil the mechanisms for direction-dependent bending behaviors observed.

2. Materials and methods

2.1. Bio-inspiration

Common millet is a crop found worldwide. The key to a crop's survivability is its reproduction. Here we take a closer look at the seeds of this crop, more specifically the seedcoat. The seedcoat needs to provide different levels of protection under external and internal loadings. For example, the seedcoat needs to provide excellent protection when subjected to external loading such as insect or bird biting and crushing, while it only needs to provide a low level of resistance under loading from the germination and growth of the seed from inside (figure 1(a)). By removing the seed from the seedcoat, shown in figure 1(b), and taking a closer look at the microstructure of the seedcoat under an optical microscope, it is found that the exterior surface of the seedcoat consists of a layer of epidermal cells in a rectangular tile like morphology intertwined via a network of sutural interfaces. However, examining the inner surface of the seedcoats shows that the rectangular tile like morphology is still present, but with the absence of the sutural interfaces, indicating the complicated asymmetric 3D articulation of the epidermal cells with articulation complexity increases from interior surface to exterior surface. This is different from the 2D suture tessellations [6, 15, 52] which have symmetric 2D articulations about the tile mid-plane, i.e. extruding through the thickness direction.

2.2. Specimen design

The tiled composites designed include two layers: the layer comprised of hard tiles (Tile Layer), and the Soft Layer. The two coordinate systems defined, as shown in figure 2(a), are the x–y local coordinate system aligned with the tile edges, and the X–Y global coordinate system aligned with the edges of the specimens. Figure 2(a) shows that one side of the Tile Layer is fixed to the Soft Layer. There are two types of tile geometries, square base tile (BT) and tiles with suture teeth (ST). The suture tile can be considered as BT plus 3D teeth and channels. The teeth and channels have 3D matching geometries (figure 2(b)), and each tooth-channel pair can have relative sliding after contact. The tiles are arranged with an initial separation g to facilitate 3D printing.

Figure 2(b) shows the suture tile of the ST design and the important geometric parameters, consisting of the tile edge length L, the tooth base length b, the height of the tooth h, and the tile thickness H. Each tooth and channel pair is perpendicular to the tile edge. The tiles used in this study have a thickness $H = 4$ mm and an edge length $L = 7.07$ mm. The tooth base length b is $L/4$ (1.77 mm) and the height of the tooth h is $L/2.2$ (3.12 mm). The Soft Layer has a thickness of 1 mm, resulting in a total composite thickness of 5 mm.

Figure 2(c) shows the two bending directions that we will explore: bending direction 1 (D1) and bending direction 2 (D2), having an angle of 45 degrees between them. The bending resistance is desired for all combinations of tile geometry (BT or ST), in-plane bending direction (D1 or D2), and out-of-plane bending set-up (Soft-UP, SU, defined as the indenter is in contact with the soft layer of the specimen; and Soft-Down, SD, defined as the indenter is in contact with the tile layer of the specimen). This results in a total of eight different cases in bending utilizing four unique specimens as summarized in table 1.

Figure 2(d) shows portions of each tile design and direction with their cross-sections exposed. The tiles along the cross-section are highlighted with alternating colors, and one tile from each is hidden to further depict the arrangement of the tiles and their dependence on their neighbors.

The specimens are fabricated via a multi-material 3D printer (Stratasys, Connex3). As shown in figure 2(e), the overall dimensions of each sample are 100 mm × 35 mm × 5 mm. The tiles are printed with a hard polymeric material Vero White (with Young's modulus of ∼2 GPa), while the soft layer is printed with a soft rubbery material TangoPlus (with Young's modulus of less than ∼1 MPa).

2.3. Bending under self-weight

The unique arrangement of the Tile Layer and how it is fixed to the Soft Layer results in a material that has different amounts of flexibility in different directions. For all eight cases, due to gravity alone, the deformation of the specimens about a cylindrical surface of radius $r = 21.5$ mm is shown from the side view and from the top view in figures 3(a) and (b) respectively. It can be seen that under the self-weight the BT and ST designs show similar level of flexibility for each direction (D1 and D2) and orientation (with the cylinder

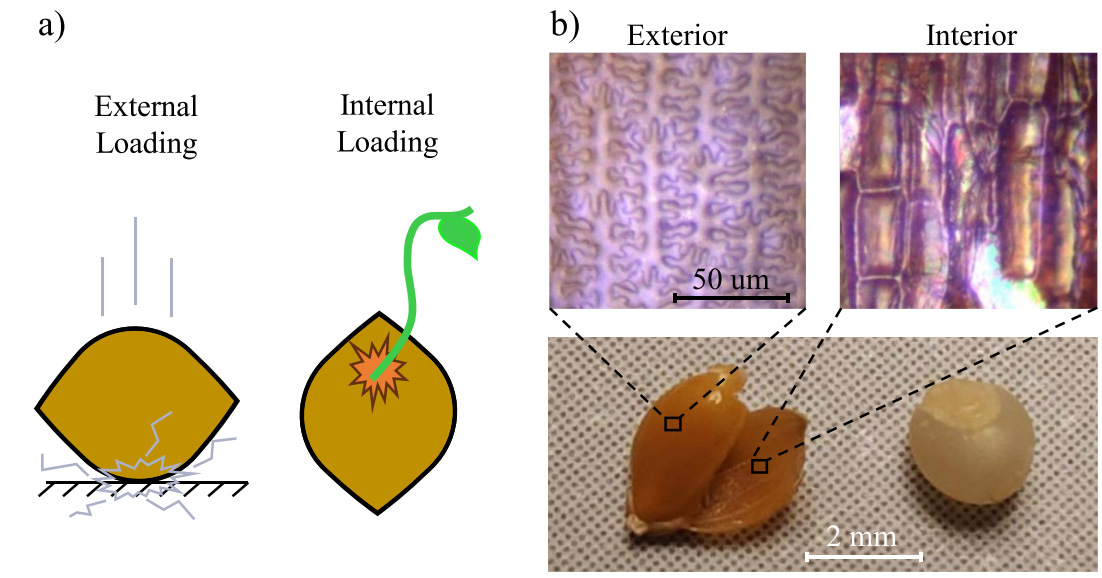

Figure 1. (a) Schematics of external versus internal loading on the common millet seedcoat, (b) removal of the seed from the seedcoat along with imaging of the exterior and interior surfaces of the seedcoat under an optical microscope.

in contact with the soft layer, and with the cylinder in contact with the tile layer).

In general, the D1 specimens (with both BT and ST designs) with the Soft Layer in contact with the cylindrical surface results in a larger curvature than the corresponding D2 specimens, as shown in figures 3(a) and (b). Also, for each design with the tile side in contact with the cylindrical surface, the specimens show much smaller curvature and do not conform to the cylindrical surface. For the case in which the cylinder is in contact with the tiles, it is seen that the samples have a slight curvature to them and that all tiles are currently contacting each other (a result of their self weight). This results in a stiffening behavior discussed in detail later on, but it should be noted that if the sample is initially flat with the tiles not initially in contact, the samples will be more flexible and display similar properties to that of the soft layer.

2.4. Three-point bending mechanical experiments of 3D-printed samples

Three-point bending experiments are performed on one sample for each combination of tile geometry, bending direction and bending set-up, with each of the eight cases summarized in table 1. The two bottom supports are spaced 60 mm from each other with the top indenter tip centered between them. The samples are centered on the supports leaving 20 mm of overhang on each end. The experiments are conducted by using the Instron 6800 Series Universal Testing System and are performed at a quasi-static testing rate of 1 mm min^{-1}. Images are taken at even intervals to observe the deformation and failure of the samples. Deflections of zero represent the initial configuration of the sample at rest, not necessarily coinciding with a flat sample configuration. Samples are loaded until failure, until constant sliding of the sample between the supports is observed, or until the sample slides off the supports (for the extremely flexible sample cases).

The bending rigidity of each case will be quantified experimentally by calculating the materials flexural modulus, E_F, using equation (1), where L_s is the support span, w is the sample width, d is the sample thickness, m is the slope of the load deflection curve.

$$E_F = \frac{L_s^3 m}{4wd^3}. \quad (1)$$

The bending strength of each case will be quantified via the maximum force obtained during the three-point bending experiments, F_{max}.

2.5. Additional methods of analysis

To both explain and verify the results observed in the three-point bending experiments, additional methods of analysis are performed and detailed in the supplementary document. An analytical analysis aimed at quantifying the influence that the tooth channel pairs have on the overall strength and deflection at failure for the soft-down D1 loading case is shown in section SA of the supplementary document.

As it is well known that bending behavior induces local tension and compression, the behavior of the sample under uniaxial tension are explored. VeroWhite grips are added, and samples are 3D-printed for experiments, again using the Instron 6800 Series Universal Testing System at a quasi-static loading rate of 1 mm min^{-1} until failure. FE models of the RVEs of all designs are created in ABAQUS/CAE,

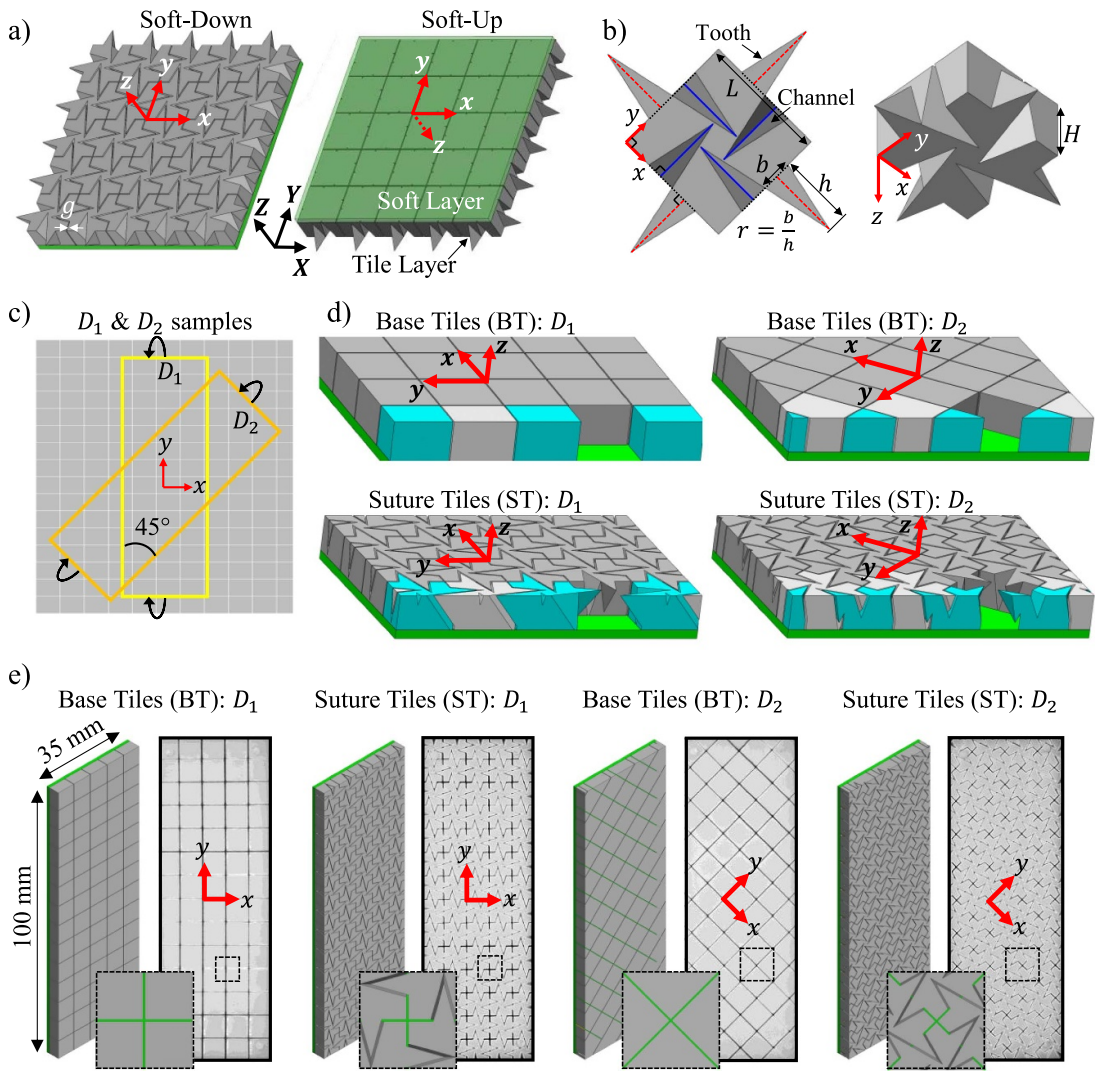

Figure 2. Specimen designs. (a) the Soft-Down and Soft-Up views of the design, (b) 3D suture tile geometry, (c) outlines of sample with two bending directions D1 and D2, (d) cross section views of each tile geometry and each bending direction, (e) the designed and 3D printed specimens.

Table 1. Summary of the eight cases of three-point bending experiments.

Case number	1	2	3	4	5	6	7	8
Tile geometry	BT	ST	BT	ST	BT	ST	BT	ST
Direction	D1	D1	D2	D2	D1	D1	D2	D2
Bending set-up	SU	SU	SU	SU	SD	SD	SD	SD

and are subjected to periodic boundary conditions for comparison with the uniaxial tension experimental results. These methods and results are detailed in section SB of the supplementary document.

Finally, an analysis on the rotation and sliding of the three-point bending samples about the supports is performed in which both the experimental data and image analysis of the experiments are used in tandem to verify the end of test modes for each sample, described in section SC of the supplementary document.

3. Three-point bending results and discussions

3.1. Soft-up cases (cases 1-4)

Figure 4(a) shows a schematic of the experimental setup while figures 4(b)–(e) show the experimental results for the Soft-Up cases for D1 and D2 specimens, respectively. As shown in figure 4(b), when loaded Soft-Up, both BT-D1 and ST-D1 specimens are highly flexible and share similar peak loads and final displacements. The samples are so flexible that they

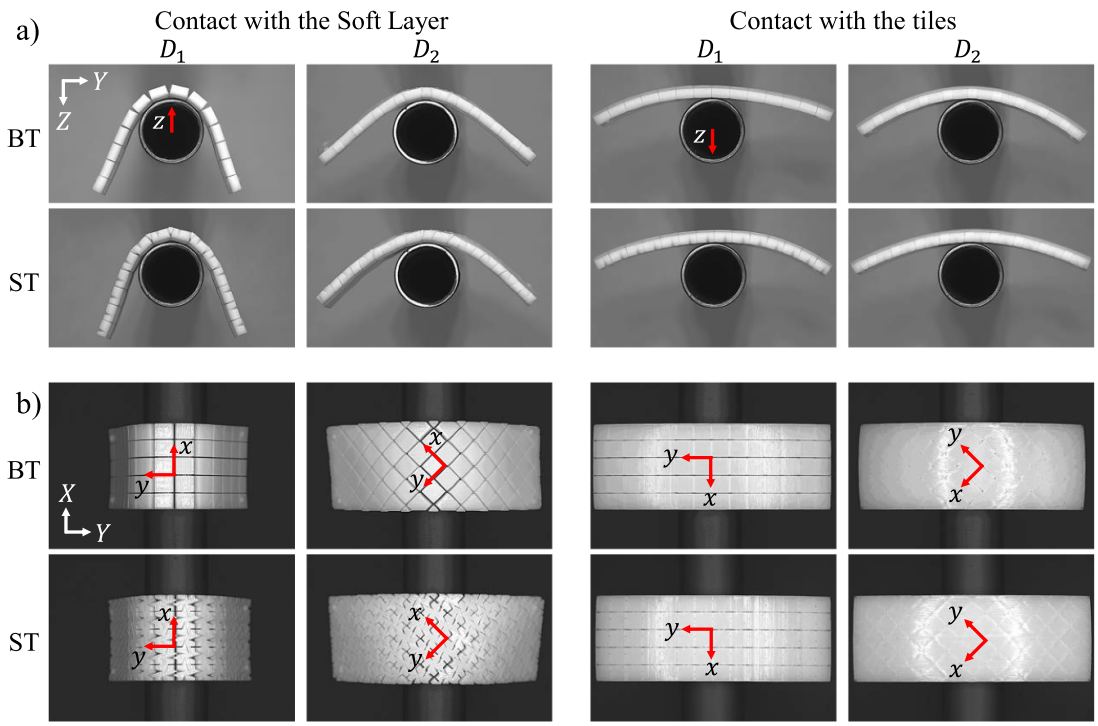

Figure 3. The deformation of the specimens about a cylindrical surface of radius $r = 21.5$ mm for all eight cases under self-weight only, (a) the side view and (b) the top view.

are being held up in place the friction between the supports and the tiles. When the load drops to zero the samples have deflected enough through the supports that the friction is not enough to support them and they collapse under their own weight without failure.

As shown in figure 4(d), for Soft-Up D2 specimens, ST-D2 reaches a 3.79 times higher force than that of BT-D2, and both end up sliding. Similar to the uniaxial tensile results in section SB of the supplementary document, there is an initial region where both ST and BT share the same bending rigidity, that of only the soft layer, but after enough deformation has occurred in the ST design, the tooth-channel pair come in contact, forcing the negative Poisson's ratio and causing an increase in bending rigidity for ST. Figures 4(c) and (e) show the images during the last point in testing along with post–experimental images of the samples. For all cases 1–4, the samples were not damaged after the bending tests.

3.2. Soft-Down cases (cases 5–6)

The ST-D1 and BT-D1 show similar bending rigidity but ST-D1 reaches a 1.31 times larger force and a 1.72 times larger displacement at failure than the BT-D1 design. The images of the last point of experimentation and the post-experimental images of the samples in figures 5(c) and (d), show that soft layer failure occurs for the Soft-Down cases in D1 direction for both BT and ST. No change in bending rigidity is observed between BT and ST after the tiles contact each other and this correlates well with the tensile experimental results for this direction, as no difference in stiffness is seen there and no auxetic behavior is measured in the direction either.

The increase in strength and deflection from the BT design to the ST can be quantitatively explained via the analytical analysis in which the interacting forces of two neighboring tiles and the thein layer connecting them are analyzed as a function of the tile's articulation angle, Θ (full derivation in section SA of the supplementary document). Figure 6(a) shows the cross section of the BT and ST tiles depicting the articulation angle $\Theta = 0$ for BT and $\Theta = 38.8°$ for ST. Figure 6(b) shows how the articulation angle of the tile can increase the designs deflection compared to that of $\Theta = 0$, for the same interacting forces in the soft layer. This means that when this interacting force reaches a critical level to cause failure for each case, the articulated tiles will experience the shown scalar increase in deflection compared to that of the $\Theta = 0$ case.

The analytical results show that the ST design should see a 1.62 times larger deflection than the BT design. Assuming the critical load occurs at the peak force experimentally, the analytical model matches closely with the experimental results that show the ST design reaches a 1.68 times larger deflection than BT at the initiation of failure.

For the case of linear elastic material properties, the deflection will be linearly related to the overall

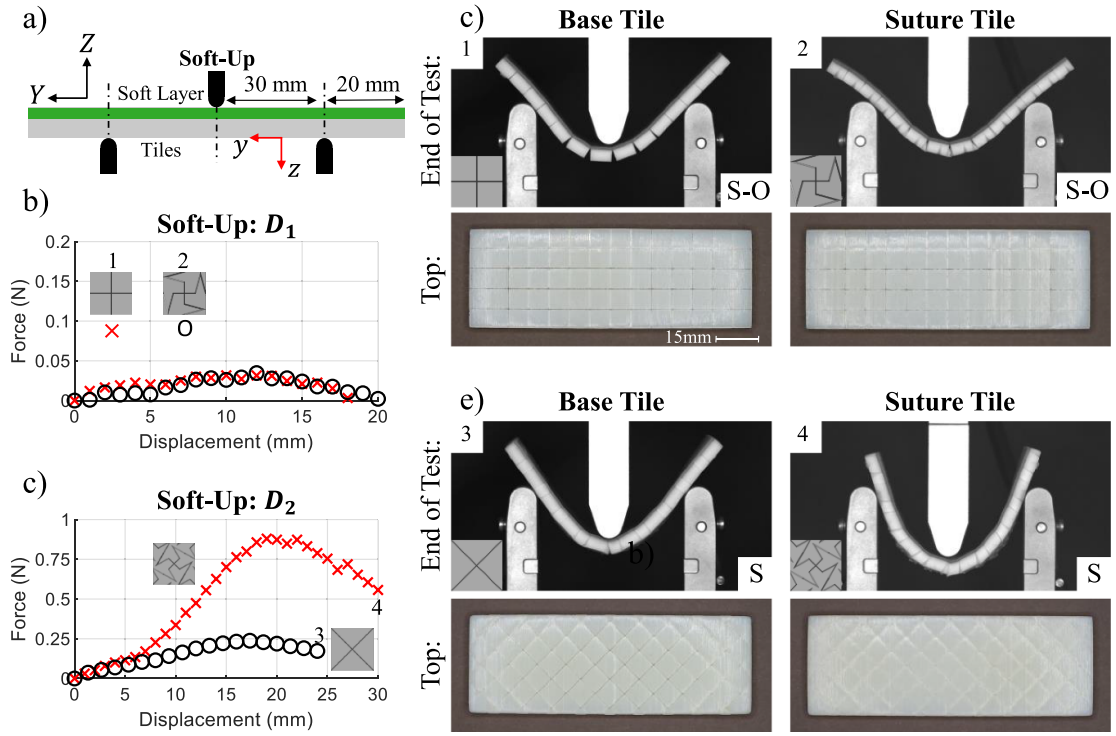

Figure 4. Three-Point bending experimental results (Soft-UP, Cases 1–4). (a) The Soft-Up three-point bending experimental set up. (b) Load-displacement curves, and (c) images at the final deflection during the experiment and images of the post-experiment samples of the D1 specimens with BT and ST. (d) Load-displacement curves, and (e) images at the final deflection during the experiment and images of the post-experiment samples of the D2 specimens with BT and ST.

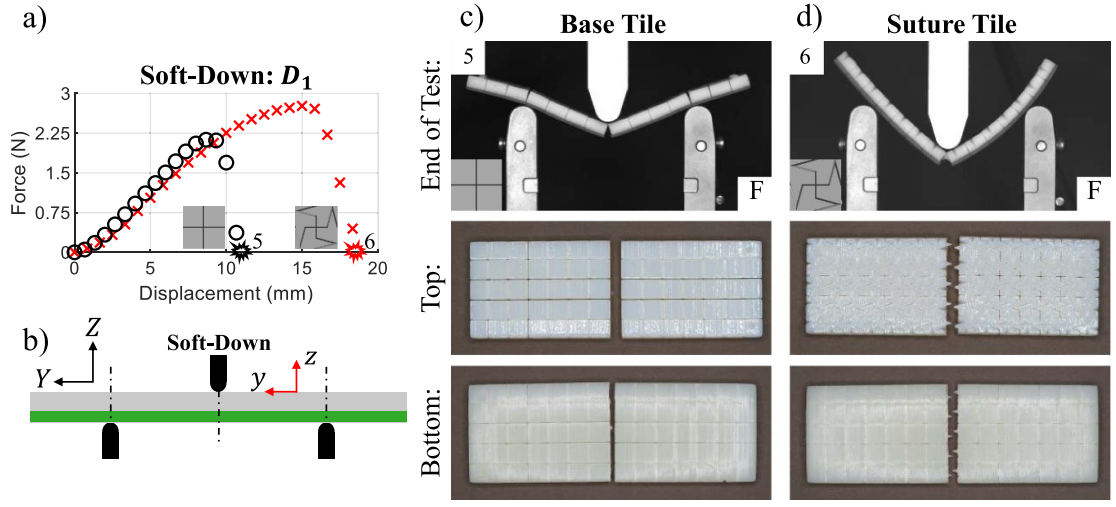

Figure 5. Three-Point bending experimental results (Soft-Down, Cases 5–6). (a) The Soft-Down three-point bending experimental set up. (b) Load-displacement curves, and (c) images at the final deflection during the experiment and images of the post-experiment samples of the D1 specimens with BT and ST.

load and bending moment, meaning both would also see this 1.62 times increase from BT to ST, however only a 1.31 times increase is observed experimentally due to the hyperelastic material properties of the soft layer.

In short, the increase in articulation angle results in a decrease in the interacting forces acting on the tile, which both increases the deflection and bending strength, and it is expected that both can be further increased when the articulation angle Θ increases further.

3.3. Soft-down cases (cases 7–8)

Figure 7 shows the Soft-Down three point bending experimental results for D2 specimens. When loaded with Soft-Down, ST-D2 shows a 2.22 times higher

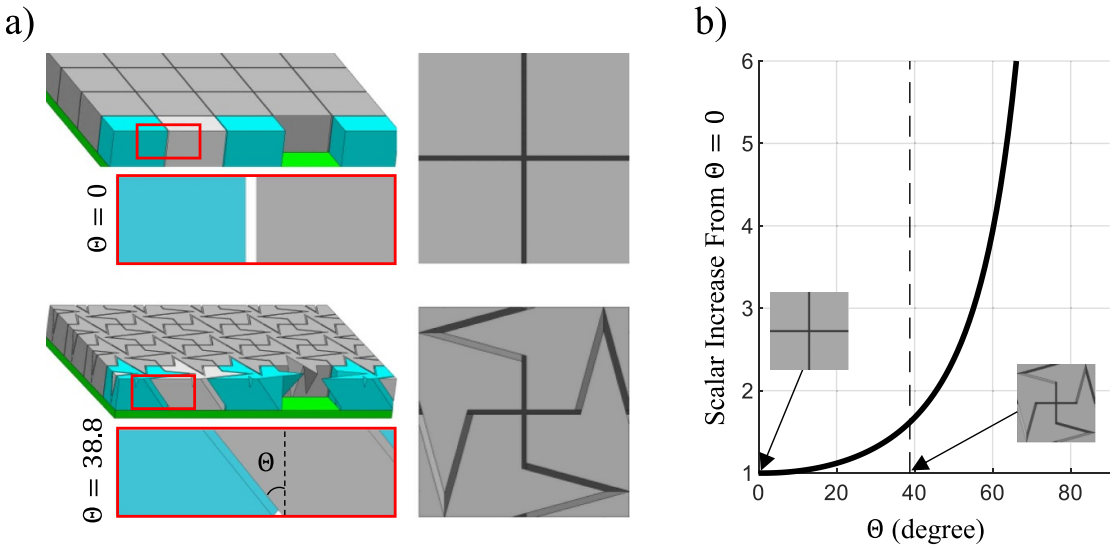

Figure 6. Analytical analysis on the influence of the articulation angle of the designs bending strength and deflection at failure. (a) Schematics of the tile's cross section depicting the articulation angel for the BT and ST designs (b) the scalar increase in the designs overall deflection compared to $\Theta = 0$ as a function of the articulation angle.

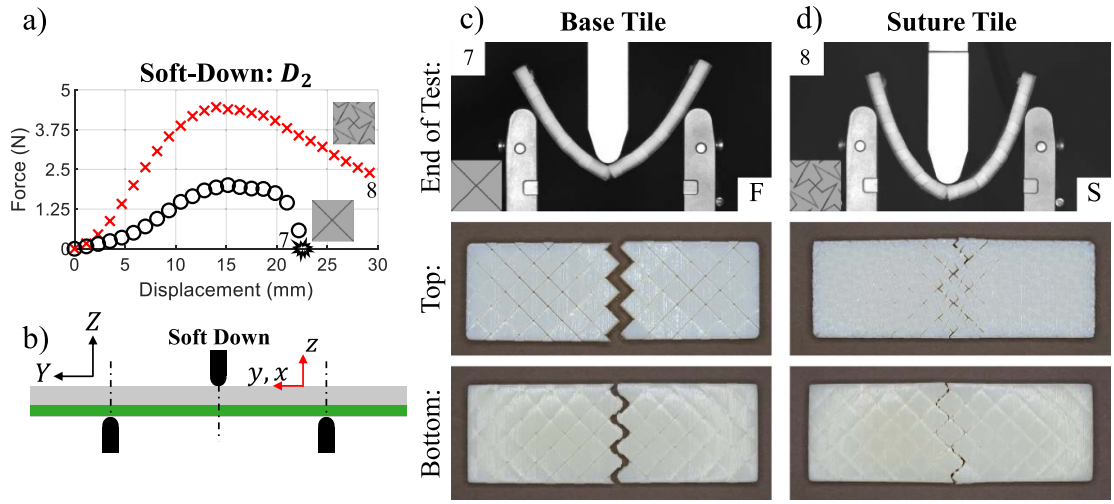

Figure 7. Three-point bending experimental results (Soft-Down, Cases 7–8). (a) The Soft-Down three-point bending experimental set up. (b) Load-displacement curves, and (c) images at the final deflection during the experiment and images of the post-experiment samples of the D2 specimens with BT and ST.

force than that of BT-D2. The soft layer for ST-D2 damages but does not experience total failure, thus the designs and end up sliding, while the soft layer in BT-D2 ends up fractured, shown in the post experimentation images. ST and BT specimens show a similar bending rigidity early on but once contact between tiles occur, the ST design quickly increases its bending rigidity compared to the BT design. The tooth-channel contact and the negative Poisson's ratio in the ST design provide a mechanism to increase the interaction between tiles and in turn the soft layer while neither is present in the BT design. The tensile result for this direction highlights this effect with the increase in stiffness and strength, and the introduction of negative Poisson's ratio observed for the ST design once contact has been made.

Although an analytical analysis on bending in the D2 direction is not conducted (due to the complexity introduced by no longer being able to approximate it as a 2D problem), the concepts are still applicable. The introduction of teeth-channel pairs allows for more of the load to be distributed from the soft layer into the tile layer. The negative Poisson's ratio activates more of the surrounding tiles to resist the load. The combination of the two enable the ST design to distribute even more of the indentation load from the soft layer to the tiles, resulting in a significant increase in not only bending rigidity, but also the bending strength and deformation for final failure/sliding. The absence of total failure in the soft layer for the ST design further exemplifies the benefits of the negative Poisson's ratio and articulated tooth-channels.

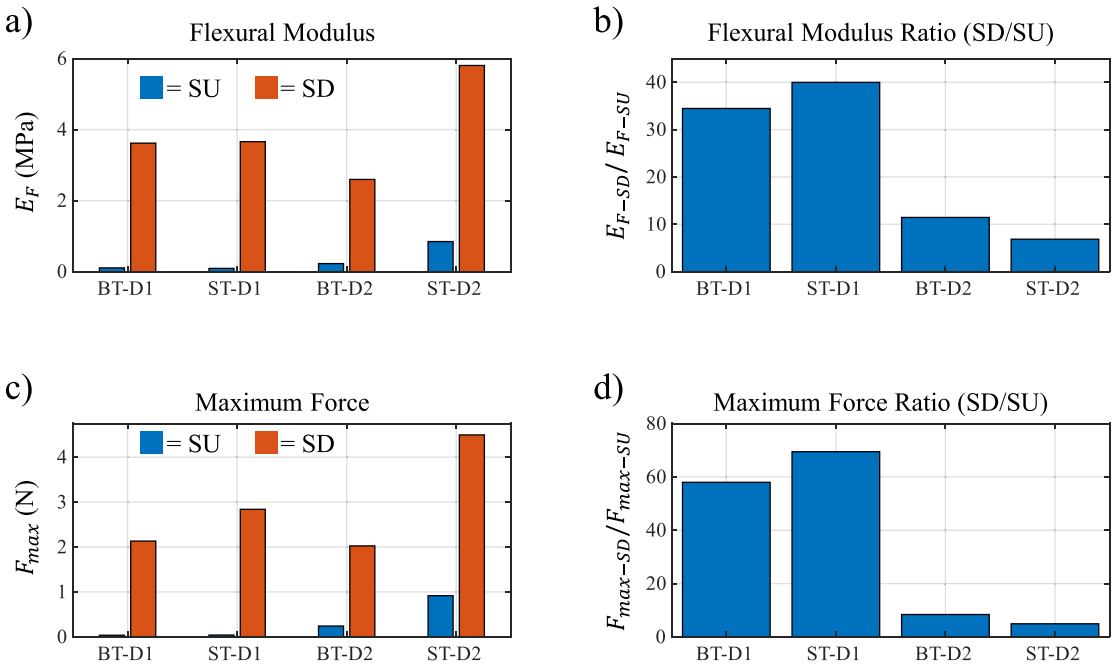

Figure 8. Comparison of flexural modulus and maximum force for the eight cases. (a) A bar plot of the flexural modulus for each of the eight cases, (b) a bar plot of the ratio of SD flexural modulus to SU flexural modulus for each tile geometry and bending direction, (c) a bar plot of the maximum force for each of the eight cases, (d) a bar plot of the ratio of SD maximum force to SU maximum force for each tile geometry and bending direction.

Table 2. Summary of the final modes of all three-point bending experiments.

Case number	1	2	3	4	5	6	7	8
Tile geometry	BT	ST	BT	ST	BT	ST	BT	ST
Direction	D1	D1	D2	D2	D1	D1	D2	D2
Bending set-up	SU	SU	SU	SU	SD	SD	SD	SD
End of test	S-O	S-O	S	S	F	F	F	S

3.4. Design comparisons

Figure 8 contains comparative bar plots of both the flexural moduli and maximum force for the eight cases of three-point bending experiments. Figure 8(a) shows the flexural modulus and for all designs and directions, the SD bending orientation shows much larger bending rigidity than the SU bending orientation, with the ST-D2 case being the stiffest. The ratio of SD to SU is shown in figure 8(b), where the ST design holds both the largest ratio (for D1) and the smallest ratio (for D2).

Compared with ST-D1 design, under Soft-Down bending, ST-D2 design not only shows increased bending rigidity but also show a significantly increased bending strength, while for ST-D1 design, the bending rigidity is similar to that of BT-D1 design. This indicates that tooth-channel pair barely influence the bending rigidity in D1 direction, but significantly influence the bending rigidity in D2 direction.

A very similar trend to the bending rigidity is seen for the strength in terms of the samples maximum force and the maximum force ratio shown in figures 8(c) and (d) respectively. Both bending rigidity and maximum force are found to have above an order of magnitude difference between the SU and SD bending orientations. The bending rigidity is so low for the SU cases that none experience damage during the experiment. For the SD cases all except ST-D2 experience fracture of the sample, despite it having the largest bending rigidity and reaching the greatest maximum force, it was able to efficiently transfer the bending load from the soft layer to the tiles.

The deflection at failure comparison is complex as there are varying end of test criteria. In general, all experiments are initially dominated by the bending deformation where the sample rotates about each lower three-point bending support. If the samples remain intact long enough this rotation phase is followed by sliding of the sample on the lower supports. Different combinations of these two processes during the experiment result in three different final modes: Sliding (S), Slide-Off (S–O), and Fracture (F), and a detailed description of how they are determined can be found in section SC of the supplementary document. The final modes of each experimental case are summarized in table 2.

Table 2 shows that no specimens fracture for Soft-Up bending. For Soft-Up bending, both BT and ST designs end up with slide-off in D1 direction and gradual sliding in D2 direction. For Soft-Down bending, BT designs fracture in both D1 and D2 directions, while ST designs fracture in D1 direction but not in D2 direction.

4. Conclusions

In summary, all the tiled composites explored show direction dependent bending properties. Under three-point bending, all designs have a much higher bending rigidity and reach a much higher bending strength when loaded Soft-Down than when loaded Soft-Up. The difference in bending rigidity from SD to SU is maximized for bending direction D1 with ratios of over 30, and is minimized for bending direction D2 with ratios under 20, with the ST design holding both the maximum and minimum ratio.

The lack of negative Poisson's ratio in the D1 bending direction (as determined from the tensile tests in section SB of the supplementary document) result in no additional tiles activated in resisting the bending load for ST compared to BT, resulting in very similar bending rigidity. This means that the addition of 3D articulation in the tiles does not affect the composite's flexibility in this direction. It was also shown for the D1 direction, both analytically and experimentally, that this addition will increase the deflection and bending strength at damage initiation without sacrificing the bending rigidity. The analytical model shows that benefits can be enhanced in designs with even larger articulation angles, Θ, further reducing local forces on the tiles and the local internal forces in the soft layer connecting neighboring tiles.

In the D2 bending direction the negative Poisson's ratio in the ST design plays an important role of activating more of the tile layer to resist the bending load, effectively increasing the bending rigidity, and reducing the load in the soft layer, effectively increasing the deflection at damage initiation, and bending strength. These effects are highlighted by the fracture seen in the soft layer for all SD designs except the ST-D2 design, where the soft layer damages, but remains connected. For the SD case, deflection at failure is significantly increased from bending directions D1 to D2 and again for BT to ST. The SU cases have such low bending rigidities that they do not fail and the deflection at failure is not quantifiable.

The 3D articulated tiled composite provides an excellent way to obtain variable bending behaviors due to its direction-dependent properties. An order of magnitude difference in bending rigidity and strength are obtainable between the SU and SD bending orientations, while finer tuning in these properties is obtainable by rotation of the composite from bending direction D1 to D2, all within a single material. Altering the 3D articulation of the tiles can result in custom negative Poisson's ratio and custom articulation angle, further enhancing the composite properties and merits additional studies.

Data availability statement

All data that support the findings of this study are included within the article (and any supplementary files).

Acknowledgments

This work was supported by NSF through Grant CMMI-2140223, SPARK funding, and the start-up funding from Northeastern University.

ORCID iDs

Richard J Nash https://orcid.org/0009-0004-4540-1964
Yaning Li https://orcid.org/0000-0002-8789-7900

References

[1] Ortiz C and Boyce M C 2008 Bioinspired structural materials *Mater. Sci.* **319** 1053–4
[2] Liu P, Zhu D, Yao Y, Wang J and Bui T Q 2016 Numerical simulation of ballistic impact behavior of bio-inspired scale-like protection system *Mater. Des.* **99** 201–10
[3] Ghosh R, Ebrahimi H and Vaziri A 2014 Contact kinematics of biomimetic scales *Appl. Phys. Lett.* **105** 233701
[4] Duro-Royo J, Zolotovsky K, Mogas-Soldevila L, Varshney S, Oxman N, Boyce M C and Ortiz C 2015 MetaMesh: a hierarchical computational model for design and fabrication of biomimetic armored surfaces *Comput.-Aided Des.* **60** 14–27
[5] Song J 2011 *Multiscale Materials Design of Natural Exoskeletons: Fish Armor* (Massachusetts Institute of Technology)
[6] Hasseldine B, Gao C and Li Y 2019 Prediction of the anisotropic damage evolution of dry common millet (Panicum miliaceum) seed under quasi-static blunt indentation *Eng. Fract. Mech.* **214** 112–22
[7] Danin A and Bagella S 2012 A new cultivar microspecies of the Portulaca oleracea aggregate from the E Mediterranean *Willdenowia* **42** 63–65
[8] Achrai B and Wagner H D 2015 The red-eared slider turtle carapace under fatigue loading: the effect of rib–suture arrangement *Mater. Sci. Eng.* **53** 128–33
[9] Sherman V R, Yaraghi N A, Kisailus D and Meyers M A 2016 Microstructural and geometric influences in the protective scales of Atractosteus spatula *J. R. Soc. Interface* **13** 2016059
[10] Zhu D, Ortega C F, Motamedi R, Szewciw L, Vernerey F and Barthelat F 2012 Structure and mechanical performance of a "modern" fish scale *Adv. Eng. Mater.* **14** 185–94
[11] Rawat P, Zhua D, Rahmanc M Z and Barthelat F 2021 Structural and mechanical properties of fish scales for the bio-inspired design of flexible body armors: a review *Acta Biomater.* **121** 41–67
[12] Sherman V R, Quan H, Yang W, Ritchie R O and Meyers M A 2017 A comparative study of piscine defense: the scales of Arapaima gigas, Latimeria chalumnae and Atractosteus spatula *J. Mech. Behav. Biomed. Mater.* **73** 1–16
[13] Jiang S, Liu J, Xiong W, Yang Z, Yin L, Li K and Huang Y 2022 A snakeskin-inspired, soft-hinge kirigami metamaterial for self-adaptive conformal electronic armor *Adv. Mater.* **34** 220409

[14] Li Y, Ortiz C and Boyce M C 2011 Stiffness and strength of suture joints in nature *Phys. Rev.* E **84** 062904
[15] Gao C, Hasseldine B, Li L, Weaver J C and Li Y 2018 Amplifying strength, toughness, and auxeticity via wavy sutural tessellation in plant seedcoats *Adv. Mater.* **30** 1800579
[16] Gao C and Li Y 2019 Mechanical model of bio-inspired composites with sutural tessellation *J. Mech. Phys. Solids* **122** 190–204
[17] Hasseldine B, Gao C, Collins J M, Jung H, Jang T, Song J and Li Y 2017 Mechanical response of common millet (Panicum miliaceum) seeds under quasi-static compression: experiments and modeling *J. Mech. Behav. Biomed. Mater.* **73** 102–13
[18] Lu H, Zhang J, Wu N, Liu K, Xu D and Li Q 2009 Phytoliths analysis for the discrimination of foxtail millet (Setaria italica) and common millet (Panicum miliaceum) *PLoS One* **4** e4448
[19] Sharabi M, Varssano D, Eliasy R, Benayahu Y, Benayahu D and Haj-Ali R 2016 Mechanical flexure behavior of bio-inspired collagen-reinforced thin composites *Compos. Struct.* **153** 392–400
[20] Kumar V A, Caves J M, Haller C A, Dai E, Liu L, Grainger S and Chaikof E L 2013 Acellular vascular grafts generated from collagen and elastin analogs *Acta Biomater.* **9** 8067–74
[21] Häsä R and Pinho S T 2019 A novel aluminium/CFRP hybrid composite with a bio-inspired crossed-lamellar microstructure for preservation of structural integrity *Compos. Sci. Technol.* **182** 107760
[22] Häsä R and Pinho S T 2019 Failure mechanisms of biological crossed-lamellar microstructures applied to synthetic high-performance fiber-reinforced composites *J. Mech. Phys. Solids* **125** 53–73
[23] Hu X, Sun Z, Zhang C, Wang X and Wu K 2018 Microstructure and mechanical properties of bio-inspired Cf/Ti/Mg laminated composites *J. Magnes. Alloy* **6** 164–70
[24] Deepak S, Thirumalaikumarasamy D, Ashokkumar M and Nayak S K 2022 Experimental analyzing the static puncture resistance performance of shear thickening fluid impregnated polypropylene hybrid composite target structures for armour application *J. Text. Inst.* **114** 351–63
[25] Sampathkumar D, Mohankumar A, Teekaraman Y, Kuppusamy R, Radhakrishnan A and Ghorbal A 2023 Bioinspired sandwich structure in composite panels *Adv. Mater. Sci. Eng.* **2023** 1–9
[26] Hedayati R, Guven A and Zwaag S 2021 3D gradient auxetic soft mechanical metamaterials fabricated by additive manufacturing *Appl. Phys. Lett.* **118** 141904
[27] Kadic M, Milton G W, Hecke M and Wegener M 2019 3D metamaterials *Nat. Rev. Phys.* **1** 198–210
[28] Lee J, Singer J P and Thomas E L 2012 Micro-/nanostructured mechanical metamaterials *Adv. Mater.* **24** 4782–810
[29] Wenz F, Schmidt I, Leichner A, Lichti T, Baumann S, Andrae H and Eberl C 2021 Designing shape morphing behavior through local programming of mechanical metamaterials *Adv. Mater.* **33** 2008617
[30] Mirzaali M J, Janbaz S, Strano M, Vergani L and Zadpoor A A 2018 Shape-matching soft mechanical metamaterials *Sci. Rep.* **8** 965
[31] Shen J, Zhou S, Huang X and Xie Y 2014 Simple cubic three-dimensional auxetic metamaterials *Phys. Status Solidi* b **251** 1515–22
[32] Mizzi L, Azzopardi K M, Attard D, Grima J N and Gatt R 2015 Auxetic metamaterials exhibiting giant negative Poisson's ratios *Phys. Status Solidi Rapid Res. Lett.* **9** 425–30
[33] Faraci D, Driemeier L and Comi C 2021 Bending-dominated auxetic materials for wearable protective devices against impact *J. Dyn. Behav. Mater.* **7** 425–35
[34] Shi T, Zhang X, Hao H and Xie G 2021 Experimental and numerical studies of the shear resistance capacities of interlocking blocks *J. Build. Eng.* **44** 103230
[35] Brighenti R 2014 Smart behavior of layered plates through the use of auxetic materials *Thin-Walled Struct.* **84** 432–42
[36] Mahdia S and Gillespie J W 2004 Finite element analysis of tile-reinforced composite structural armor subjected to bending loads *Composites* B **35** 57–71
[37] Fang H, Chu S A, Xia Y and Wang K 2018 Programmable self-locking origami mechanical metamaterials *Adv. Mater.* **30** 1706311
[38] Huang C, Tan T, Hu X, Yang F and Yan Z 2022 Bio-inspired programmable multi-stable origami *Appl. Phys. Lett.* **121** 051902
[39] Lv C, Krishnaraju D, Konjevod G, Yu H and Jiang H 2014 Origami based mechanical metamaterials *Sci. Rep.* **4** 5979
[40] Neville R M, Scarpa F and Pirrera A 2016 Shape morphing Kirigami mechanical metamaterials *Sci. Rep.* **6** 31067
[41] Babaee S, Shim J, Weaver J C, Chen E R, Patel N and Bertoldi K 2013 3D soft metamaterials with negative poisson's ratio *Adv. Mater.* **25** 5044–9
[42] Bertoldi K, Vitelli V, Christensen J and Hecke M 2017 Flexible mechanical metamaterials *Nat. Rev. Mater.* **2** 17066
[43] Porter M M, Ravikumar N, Barthelat F and Martini R 2017 3D-printing and mechanics of bio-inspired articulated and multi-material structures *J. Mech. Behav. Biomed. Mater.* **73** 114–26
[44] Wallbanks M, Khan M F, Bodaghi M, Triantaphyllou A and Serjouei A 2022 On the design workflow of auxetic metamaterials for structural applications *Smart Mater. Struct.* **31** 023002
[45] Li T, Hu X, Chen Y and Wang L 2017 Harnessing out-of-plane deformation to design 3D architected lattice metamaterials with tunable Poisson's ratio *Sci. Rep.* **7** 8949
[46] Gao C, Slesarenko V, Boyce M C, Rudykh S and Li Y 2018 Instability-induced pattern transformation in soft metamaterial with hexagonal networks for tunable wave propagation *Sci. Rep.* **8** 11834
[47] Zadeh M N, Alijani F, Chen X, Dayyani I, Yasaee M, Mirzaali M J and Zadpoor A A 2021 Dynamic characterization of 3D printed mechanical metamaterials with tunable elastic properties *Appl. Phys. Lett.* **118** 211901
[48] Jiang H, Zhang Z and Chen Y 2020 3D printed tubular lattice metamaterials with engineered mechanical performance *Appl. Phys. Lett.* **117** 011906
[49] Fu M, Chen Y, Zhang W and Zheng B 2016 Experimental and numerical analysis of a novel three-dimensional auxetic metamaterial *Phys. Status Solidi* b **253** 1565–75
[50] Pan F, Li Y, Li Z, Yang J, Liu B and Chen Y 2019 3D pixel mechanical metamaterials *Adv. Mater.* **31** 1900548
[51] Evans K and Alderson A 2000 Auxetic materials: functional materials and structures from lateral thinking! *Adv. Mater.* **12** 617–28
[52] Nash R and Li Y 2021 Experimental and numerical analysis of 3D printed suture joints under shearing load *Eng. Fract. Mech.* **253** 107912